Fabrication of larger surface area of ZIF8@ZIF67 reverse core-shell nanostructures for energy storage applications

Fabrication of larger surface area of ZIF8@ZIF67 reverse core-shell nanostructures for energy storage applications

Iqra Rabani[a*], Muhammad Shoaib Tahir[a], Sobia Nisar[b], Marc Parrilla[c], Hai Bang Truong[d,e], Minsung Kim[f] and Young-Soo Seo[a*],

[a]Department of Nanotechnology and Advanced Materials Engineering, Sejong University, Seoul- 05006, Republic of Korea

[b]Department of electronic engineering, Sejong University, Seoul- 05006, Republic of Korea

[c]A-Sense Lab, Department of Bioscience Engineering, University of Antwerp, Groenenborgerlaan 171, 2020, Antwerp, Belgium

[d]Optical Materials Research Group, Science and Technology Advanced Institute, Van Lang University, Ho Chi Minh City, Viet Nam (truonghaibang@vlu.edu.vn)

[e]Faculty of Applied Technology, School of Technology, Van Lang University, Ho Chi Minh City, Viet Nam

[f]Department of Energ y Systems Engineering, Chung-Ang University, 84 Heukseok-ro, Dongjak-gu, Seoul 06974, Republic of Korea

Correspondence email: iqra.rabani@sejong.ac.kr & ysseo@sejong.ac.kr

Abstract

The construction of uniform nanostructure with larger surface area electrodes is a huge challenge for the high-value added energy storage application. Herein, we demonstrates ZIF67@ZIF8 (core-shell) and ZIF8@ZIF67 (reverse core-shell) nanostructures using a low-cost wet chemical route and used them as supercapacitors. Pristine ZIF-67 and ZIF-8 was used as reference electrodes. Benefiting from the synergistic effect between the ZIF8 and ZIF67, the ZIF8@ZIF67 exhibited the outstanding electrochemical consequences owing to its larger surface area with uniform hexagonal morphology. As optimized ZIF8@ZIF67 nanostructure displayed the high-capacity of 1521 F/g at 1 A/g of current density in a three-

electrode assembly in 1 M KOH electrolyte compared with other electrodes. In addition, the ZIF8@ZIF67 nanostructure employed into the symmetric supercapacitors (SSCs) with 1 M KOH electrolyte in two-electrode setup and it exhibited still superior output including capacity (249.8 F/g at 1 A/g), remarkable repeatability (87% over 10,000 GCD cycles) along with high energy and power density (61.2 Wh/kg & 1260 W/kg). The present study uncovers the relationship between the larger surface area and electrocatalyst performance, supporting an effective approach to prepare favorable materials for enhanced capacity, extended lifespan, and energy density.

Keywords: ZIF-8, ZIF-67, core-shell, reverse core-shell, supercapacitors, energy density

1. Introduction

Currently, environmental pollution and serious energy crises have developed considerable concerns due to the unnecessary combustion of fossil fuels [1, 2]. To circumvent the environmental challenges and resulting energy crises, renewable and green energy resources including wind, tidal solar and tidal energy have emerged as promising candidates [3, 4]. For this purpose, the rechargeable batteries (Li-ion) and supercapacitors (SCs) plays a significant role in the electrochemical energy storage (EES) devices. Supercapacitors (SCs) are also called electrochemical ultracapacitors and have gained immense attention among other EES on the account of versatile features such as rapid charge-discharge capability, robust extended cycling life,

excellent safety, and high-power density [5-7]. SCs have been categorized in two classifications including electric double layer capacitive (EDLC) and pseudo-capacitive (PC) based on their charge storage mechanisms [8].

Generally, the EDLC stores energy through the adsorption-desorption of electrolyte ions at the electrode/electrolyte interface. However, the EDLC-based materials are largely constrained because of their low capacitance and energy density, which hinders their utilization in practical applications [9]. By contrast, the PC encompasses the Faradaic reaction and stores charges allowing too fast and reversible redox reactions, which leads to the higher capacitance and maximum levels of energy density than that of EDLC mechanism [5]. Thus, the preparation of innovative materials, nanostructures, combining the different materials, engineering, and aiming the desired material features are still a huge challenge to evaluating the SCs performance [10-12].

To this end, Metal-organic frameworks (MOFs) are a class of porous and crystalline materials which link organic ligands and inorganic clusters through the coordination bonds [13, 14]. By wise selection of organic and inorganic components, the desired architecture and tunable properties of MOFs can be attained by molecular engineering [15]. In recent years, a variety of MOFs have been studied for the variety of applications including gas storage, drug delivery, gas separation and catalysis, etc [16-18]. Furthermore, to these high value-added application, considerable efforts have been paved into the exploitation of their usage in the EES

on the account of their built-in redox metal centers, tunable pore size, highly accessible surface area and versatile functionalities [1, 19, 20].

In this regard, Ziolitic imidazole framework (ZIFs), such as ZIF-8 and ZIF-67, are a new subclass of the MOFs and composed with the bifunctional materials including the organic linkers and coordinated inorganic clusters, which can be employed both as metal precursors and as sacrificial templates [21, 22]. In addition, the ZIF-67 demonstrates the cage-like structure which is advantageous for preparing the core-shell morphology, which further facilitate shorten ions diffusion length and mass transfer additionally to its ability to host other active species in the "*small mouth- big belly*" cages as well as they also inhibit its dissolution [23, 24]. Therefore, these features of ZIF-67 have supported to be considered as auspicious candidate to fabricate and design the electrodes for SCs high-value added application [25-28].

To date, Zhengfei et al., [29] has been synthesized ZIF-67 metal-organic framework by employing various derivative strategies for the measurement of supercapacitor performance. They have fabricated asymmetric SCs, and the specific capacitance was obtained 120 F/g at 1 A/g of current density with the low energy density of 19.7 Wh/kg. Rahim et al., [30] then synthesized cobalt based ZIF-67 and explored the asymmetric SCs performance with the 23 Wh/kg of energy density at 218 W/kg of power density. In the same line, Wang et al., [31] has been prepared ammonia borane fluoride based ZIF67 through one-step solution strategy for SCs application. They found high capacitance of 1593 F/g by employing ZIF67 with the

maximum energy density of 15.1 Wh/kg at 857.1 W/kg.

Nevertheless, the use of pristine ZIF-67 in EES faces two major challenges: 1) the intrinsic low conductivity of ZIF-67 hinder the charge transfer in the framework and therefore notably restrict their electrochemical performance and 2) pristine ZIF-67 showed a limited cyclic stability with low capacitance retention [32-34]. Consequently, it is highly necessary to create an efficient way to address these difficulties that further would boost the overall charge storage performance in EES.

To this end, we have demonstrated the ZIF67@ZIF8 core-shell and ZIF8@ZIF67 revers core-shell nanostructures using a simple and cost-effective wet chemical route (**Figure 1**) and employed them as supercapacitor application. Due to the synergistic effect between the ZIF-8 and ZIF-67, the ZIF8@ZIF67 reverse core-shell nanostructure exhibit uniform structure with larger surface area improved the overall electrochemical performance in 1 M KOH electrolyte. As optimized ZIF8@ZIF67 reverse core-shell had capacity of 1521 F/g in three electrode configurations at 1 A/g of current density compared with other electrodes. In addition, the optimum ZIF67@ZIF8 and ZIF8@ZIF67 nanostructures embedded into SSCs in 1 M KOH electrolyte, and the ZIF8@ZIF67 exhibit the 249.8 F/g at the 1 A/g of current density with noticeable cycling stability (87% over 10,000 GCD at 10 A/g of current density) which is higher than ZIF67@ZIF8 (179.1 F/g). Based on these versatile features, we conclude that the ZIF8@ZIF67 reverse core-shell is a good candidate for supercapacitor application.

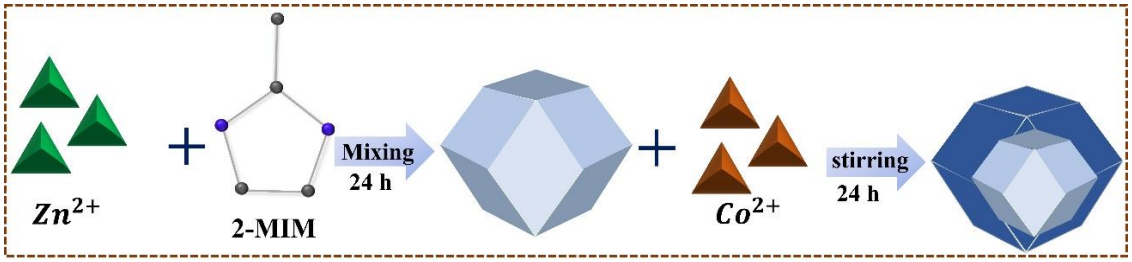

Figure 1*. Synthesis schematic illustration of the ZIF8@ZIF67 reverse core-shell.*

2. Materials and Methods

2.1. Materials

The 2-methylimidazole (2-MIM, 99%), zinc nitrate hexahydrate ($Zn(NO_3)_2.6H_2O$, 99%), polyvinyl dene fluoride (PVDF), carbon black, N-methylene propylene (NMP), ethanol (EtOH, 99.5%) and methanol (MeOH, 99%) were purchased from Sigma Aldrich, South Korea. All the chemicals were bought from the suppliers directly. The nickel foam (NF, 1.6 mm thickness) as substrate for working electrode, Nickel plate (Ni) as current collector, obtained from ALANTUM, South Korea, and they were carefully cleaned with deionized (DI) water, ethanol, and acetone.

2.2. Synthesis of the ZIF67@ZIF8 (core-shell) and ZIF8@ZIF-67 (reverse core-shell)

The core-shell and reverse core-shell hybrid were synthesized by a simple and facial wet chemical route. For synthesized the core material initially, 2-methylimidazole was dissolved in 80 mL of methanol through ultrasonication. Meanwhile, the metal salt (Zn^{2+} for ZIF-8, Co^{2+} for ZIF-67) was added and again sonicate for 5 min under the magnetically stirrer for 2 h at 500 rpm. Thereafter, the

solution was aged for the next 24 h. To prepare the shell material, a similar route with reverse material was adopted. In detail, 2-methyleimidazole was added in the precipitates of ZIF8@ZIF67 and sonicate it for 10 min to completely absorb the linker material on surface of ZIFs. Now add the corresponding metal salt (Zn^{+} for ZIF-8, Co^{+} for ZIF-67) for complete synthesis of core-shell hybrid and sonicate for 5 min under magnetically stirrer for 2 h at 500 rpm. Afterword the solution was again aged for next 24 h. The core-shell hybrid precipitates were collected by centrifugation and washed with MeOH 3 times. Dried in programable oven at 85 ^{o}C overnight. Finally, the obtained product labelled by the ZIF8@ZIF67 reverse core-shell structure and employed for the further required measurements.

2.3. Electrochemical evolution

All the measurements were performed by using the SP150 Biologic potentiostat with a standard three-electrode setup. The Hg/HgO and graphite wire were used as the reference and counter electrodes, respectively. The active material on the nickel foam was employed as the working electrode. The working electrode was fabricated by preparing the slurry of carbon black, polyvinyl dene fluoride (PVDF), and prepare material with the ratio of 10 : 10 : 80, respectively, in NMP solvent which was then decorated on the NiF and dried in the electric oven at 100 °C for overnight. The electrochemical parameters including cyclic voltammetry (CV), galvanostatic charging/discharging (GCD) and electrochemical impedance spectroscopy (EIS)

were investigated in 1 M KOH aqueous electrolyte. The specific capacitance (C) is determined based on the discharging plots by equation 1.

$$C = \frac{I \times \Delta t}{m \times \Delta V} \quad (1)$$

Where I correspondence to the current in mA, t denotes the to the discharging time in s, m and V represents the mass in mg and potential difference in volts, respectively.

2.4. Symmetric supercapacitor fabrication process

A symmetric supercapacitor was developed by sandwiching a separator (a piece of filter paper soaked with 1 M KOH electrolyte) along with the cathode and anode identical electrodes (prepared material). The electrode area was 1 cm × 1 cm, and the weight of the active material was 3 mg on the NiF substrate. Two pieces of the Ni plate was employed as a current collector. Then, the device was fabricated by employing an appropriate pressure and then used for the electrochemical measurements. The C, Energy and power density were calculated through the equation 2, 3 and 4.

$$C = \frac{2 \times I \times \Delta t}{m \times \Delta V} \quad (2)$$

$$E = \frac{C \times \Delta V^2}{8} \quad (3)$$

$$P = \frac{3600 \times E}{\Delta t} \quad (4)$$

Where E and P denotes the energy and power density.

2.5. Physical characterization

The synthesis compositions and crystallinity of the as-prepared materials were analyzing by performing the powder X-ray diffraction (XRD) analysis by employing Panalytical XRD-6100 instrument with Cu Kα radiation (λ = 1.5406 Å) at a scan speed of 5°/min; (Panalytical, Malvern, UK) in the 2θ range of 10°-80°. The morphological observations were investigated using field-emission scanning electron microscopy (FE-SEM; Hitachi (Tokyo, Japan), SU-8010, 5.0 kV, working distance: 6.8 mm) and high-resolution transmission electron microscopy (TEM; JEM-2010, 200 kV). The Raman spectra were identified through a confocal Raman microscope along with the signal wavelength of 632 nm (He-Ne source) by employing a Raman spectrometer (JASCO, NRS-3100) at ambient conditions. The surface valance states, and chemical composition analysis of the as-prepared materials were monitored through X-ray photoelectron spectroscopy (XPS) by handling a Thermoelectric Multilab-2,000 spectrometer (Al-*K*α source). The surface characteristics and porosity of the as-prepared materials were performed by means of nitrogen (N2) adsorption/desorption isotherms (BET, Micromet-rics-ASAP-2020; Micromeritics Instrument, Norcross, GA, USA).

3. Results and Discussions

3.1. Physicochemical analysis

The morphology ZIF67@ZIF8 core-shell and ZIF8@ZIF67 reverse core-shell

189 nanostructures were confirmed by TEM at low and high magnifications; and the
190 results are shown in **Figure 2(a-f)**. The micrographs for ZIF-8 and ZIF-67 exhibited
191 that they have rhombic dodecahedral morphology with smooth surface and have
192 uniform size distribution (**Figure S1-S2**). The ZIF67@ZIF8 micrographs shows little
193 disturbing morphology and also crystal size increased due to the volume increased
194 caused by the epitaxial growth. In this case, ZIF-8 was synthesized first as a core and
195 then ZIF-67 as a shell on the surface of the ZIF-8, therefore resulting in an edge of the
196 material disturbance; results are shown in **Figure 2(a-c)**.

197 In contrast, the ZIF8@ZIF67 as reverse core-shell shows the uniform size
198 distribution with smooth surface and the edges of the crystal did not show the
199 disturbance. In addition, the as obtained crystal sizes increased may be expanding
200 the volume through the epitaxial growth method and the detail results are illustrated
201 in **Figure 2(d-f)**, at low and high magnifications, respectively. In this case, the ZIF-67
202 was first synthesized as core and ZIF-8 was as shell on the surface of ZIF-67; and the
203 morphology clearly demonstrated the reverse core-shell like structure. The elemental
204 analysis and chemical composition of the ZIF67@ZIF8 core-shell and ZIF8@ZIF67
205 reverse core-shell were analyzed using EDS; and results are illustrated in **Figure 2(g-**
206 **h)**. Therefore, it is obvious from the results that the ZIF67@ZIF8 and ZIF8@ZIF67
207 were mainly composed of C (blue), N (sky blue), O (red), Co (green) and Zn (yellow).
208 Its corresponding EDS analysis was depicted in **Figure 2(g-h)**, which probes the
209 existence of the C, O, N, Zn and Co with the atomic% of 60.86, 8, 16.24, 5.62, 9.28%

and 65.66, 5.2, 14.24, 10.67, 4.23% for the ZIF67@ZIF8 and ZIF8@ZIF67, respectievly. Briefly, the ZIF8@ZIF67 was demonstrated via seed epitaxial growth because of the identical unit cell parameters of ZIF-8 and ZIF-67 (a = b = c = 16.9910 Å) [35, 36] and topological structure, which was further verified using XRD (**Figure 3a**).

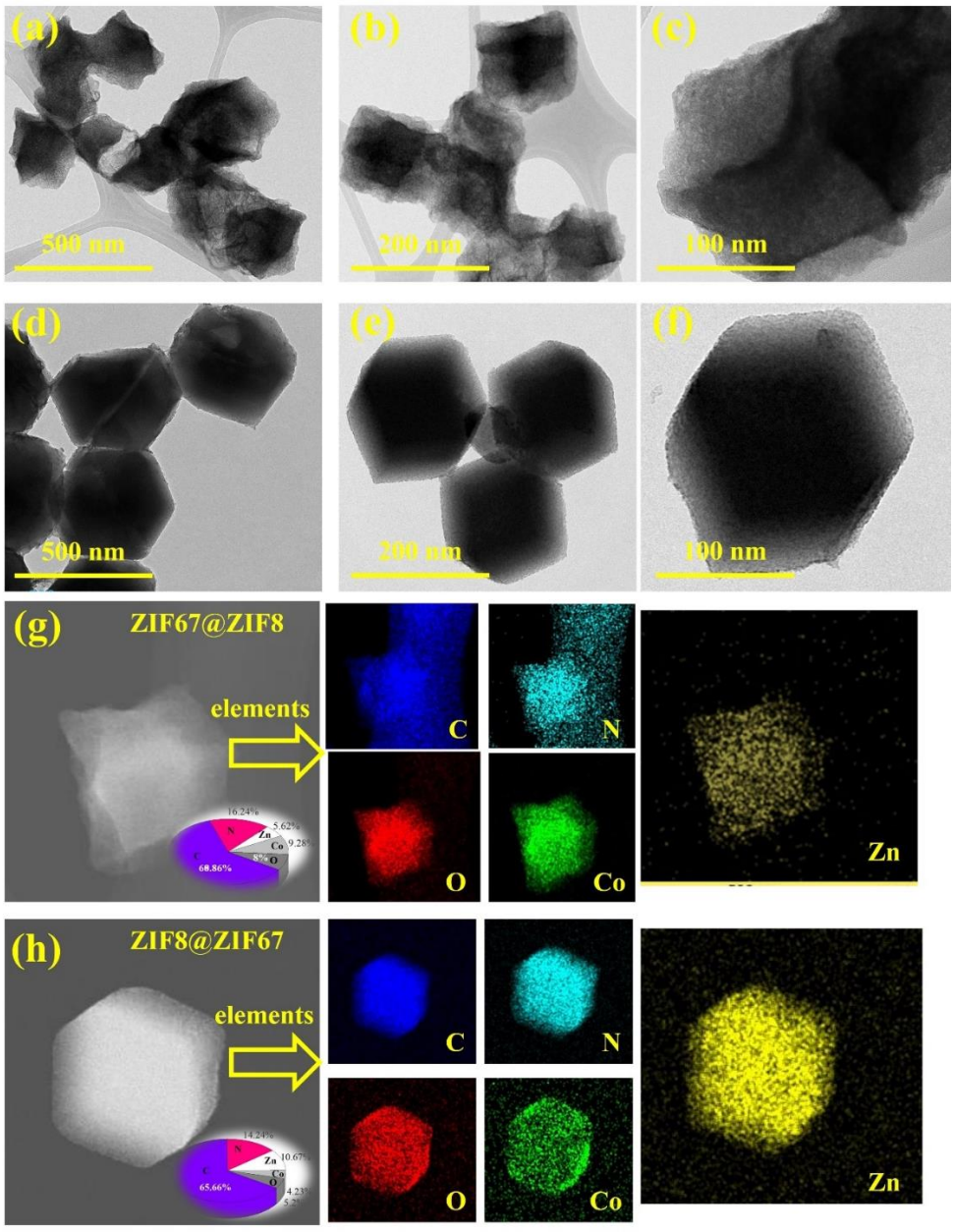

Figure 2*. TEM images at various magnifications such as* ***(a-c)*** *ZIF67@ZIF8 morphology at low and high magnifications,* ***(d-f)*** *ZIF8@ZIF67 morphology at low and high magnifications,*

*and **(g-h)** the EDX elemental mapping for the ZIF67@ZIF8 and ZIF8@ZIF67 and inset indicated the pie chart including the atomic percentage.*

The phase and crystalline structure of the ZIF67@ZIF8 and ZIF8@ZIF67 were investigated through the XRD patterns and compared with the ZIF-8 and ZIF-67; results are presented in **Figure 3**. As-prepared ZIF67@ZIF8 core-shell and ZIF8@ZIF67 reverse core-shell, the dominant reflection peaks situated at the 7.62°, 10.8°, 13.4°, 14.9°, 16.6°, 18.2°, 22.4°, 25°, 27.1°, 30.1°, 31.0°, 32.0° and 33.1° belongs to the characteristics of the crystal planes (011), (002), (112), (022), (013), (222), (114), (233), (134), (044), (244), and (235). Both nanostructures demonstrated the similar reflection peaks due to the same hexagonal morphology and the results are well matched with the state-of-the-art literature [37, 38] and the JCPDS card no. 00-062-1030 [36], which indicate the successful synthesis of all the as-prepared materials. The XRD pattern of ZIF-8 and ZIF-67 were also indicated the same pattern compared with the ZIF8@ZIF67 and ZIF67@ZIF8; and the XRD pattern is shown in **Figure 3**.

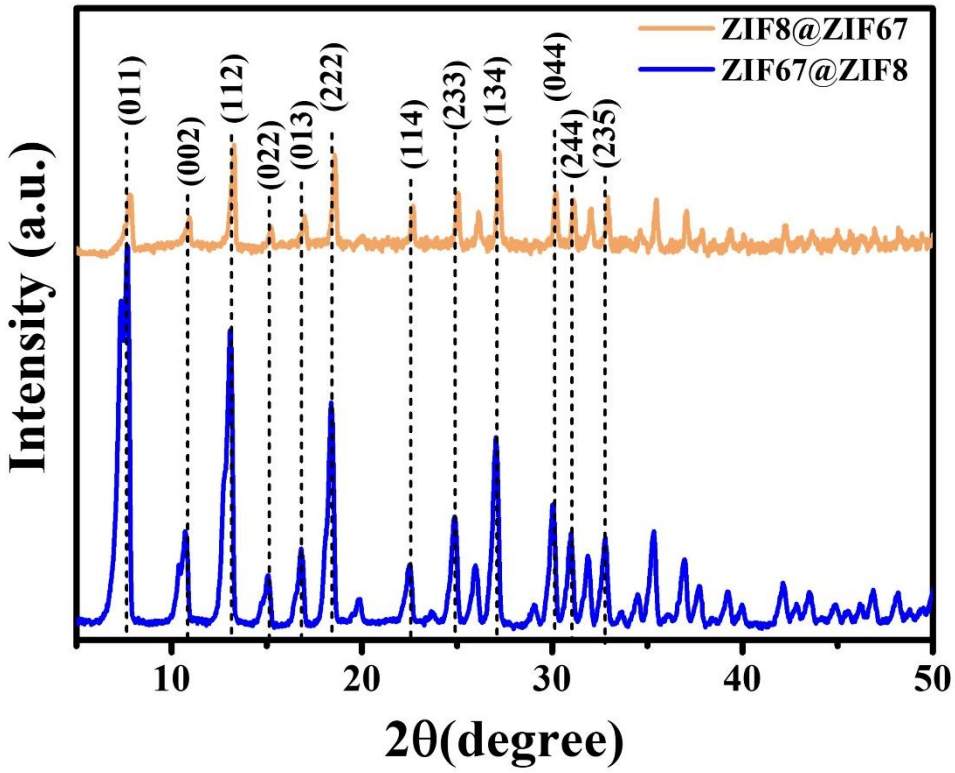

231

232 ***Figure 3**. XRD pattern for the ZIF67@ZIF8 (blue) and ZIF8@ZIF67 (peach).*

233 To further identify the chemical compositions and the surface valance state of
234 the ZIF8@ZIF67 and ZIF67@ZIF8 nanostructures, XPS analysis was conducted [39],
235 and the results are illustrated in **Figure 4**. The XPS studies of ZIF-8 and ZIF-67 were
236 also conducted (as reference samples) and the detailed results are presented in
237 **Figure S3-S4**. As **Figure S3(a)** demonstrate the overall XPS survey spectrum, which
238 confirms the presence of C 1s, N 1s, O 1s, Zn 2p elements in the pristine ZIF-8 and
239 also detailed high-resolution XPS profiles were provided in **Figure S3(b-d)**. For ZIF-
240 67, the total XPS spectrum displays in **Figure S4(a),** proving the existence of C 1s, O
241 1s, N 1s and Co 2p elements and their corresponding high resolution XPS profiles
242 were shown detailed wise in **Figure S4(b-d)**. As shown in **Figure 4(a)**, the full survey

XPS spectrum of ZIF8@ZIF67 and ZIF67@ZIF nanostructures, which confirms the presence of C 1s, O 1s, N 1s, Zn 2p and Co 2p in the resulting spectrum and the summary of the atomic percentage of elements are provided in inset **Figure 4(a)**. By Gaussian fitting process, the deconvoluted XPS high-resolution scan of the C 1s comprises two major signals attributed to the C-C and C-O at the energy levels of 284.6 eV and 286.0 eV [14] for the ZIF67@ZIF8; and the results are depicted in **Figure 4(b)**. In the case of ZIF8@ZIF67, the slight shift was noticed in the C 1s high resolution scan at the binding energy of 285.5 eV and 284.6 eV corresponds to the C-N and C-C characteristics [40], and the plot is illustrated in **Figure 4(c)**. The high resolution XPS scan of N 1s for the ZIF67@ZIF8 and ZIF8@ZIF67 can be deconvoluted into three peaks at the binding energy 398.50, 398.43 eV, 399.08, 399.4 eV and 400.9, 400.3 eV which ascribed to the pyridinic, pyrrolic, and N interacting with metals or graphitic N species (**Figure 4(d-e)**), respectievly, and the results are being consistent with the literature [13, 41]. The high-resolution XPS spectrum of Zn 2p is demonstrated in **Figure 4(f)**, wherein two deconvoluted peaks are noticed at 1020.71 eV and 1043.81 eV for the ZIF67@ZIF8, which are credited to Zn 2p3/2 and Zn 2p1/2, respectively.

According to **Figure 4(g)**, the high-resolution XPS profile was deconvoluted into two peaks at 1021.0 eV and 1044.09 eV and these peaks correspond to the Zn 2p3/2 and Zn 2p1/2, respectively, in the presence of ZIF8@ZIF67. The difference between the two bands were found to be 23.09 eV and 23.1 for the ZIF8@ZIF67 and

ZIF67@ZIF8, which signifies the presence of Zn^{+2} in both cases with slight peak shifting [42]. The high-resolution Co 2p spectrum in **Figure 4(h-i)**, two split peaks at about 780.1, 780.5 eV, and 795.9 eV, 796.2 eV are attributed to the Co $2p_{3/2}$ and Co $2p_{1/2}$ for the ZIF67@ZIF8 and ZIF8@ZIF67, respectively [43]. The difference in binding energy between these deconvoluted two peaks are about 15.4 eV and 15.7 eV, respectively. In addition, the deconvoluted two peaks at 785.2, 786.3 eV and 801.5 and 802.2 eV can be assigned to satellite peaks of Co 2p [44] and the corresponding results are illustrated in **Figure 4(h-i)**. These observed outcomes indeed clear the valence, compositions, and synthesis formation of the ZIF67@ZIF8 and ZIF8@ZIF67, nanostructures.

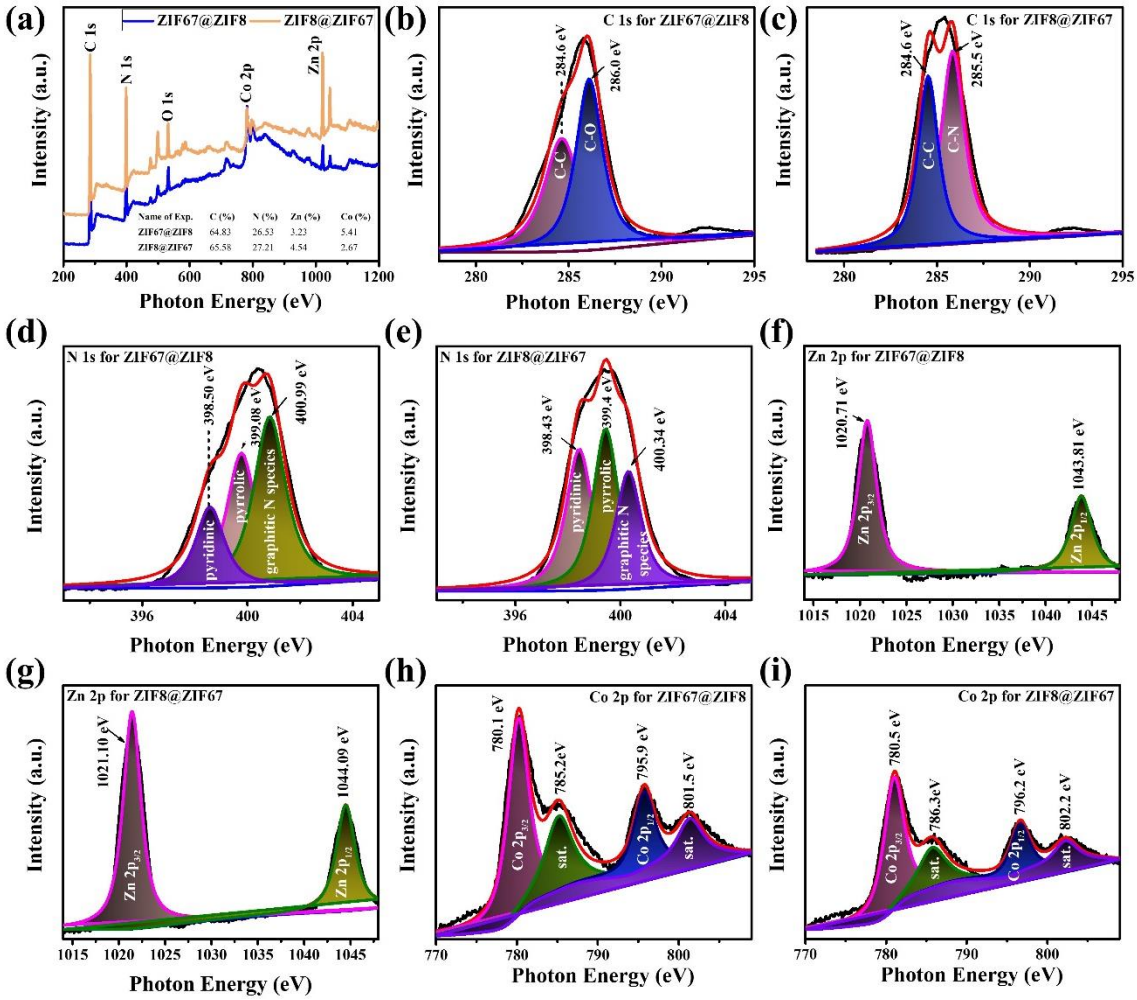

274

275 ***Figure 4****. XPS spectrums of ZIF67@ZIF8 and ZIF8@ZIF67 such as* ***(a)*** *full survey spectrum*
276 ***(b-c)*** *high-resolution C 1s spectrum,* ***(d-e)*** *high-resolution N 1s spectrum,* ***(f-g)*** *high-*
277 *resolution Zn 2p spectrum and* ***(h-i)*** *high-resolution Co 2p spectrum.*

278 To probe the specific surface area and pore volume of ZIF-8, ZIF-67,
279 ZIF67@ZIF8 and ZIF8@ZIF67 nanostructures, BET measurement was performed, and
280 the results are shown in **Figure 5**. The nitrogen (N_2) adsorption-desorption isotherms
281 of the ZIF-67, ZIF67@ZIF8 and ZIF8@ZIF67 demonstrated a similar hysteresis loop,
282 which confirms a similar porosity as the results are illustrated in **Figure 5(a)**. They
283 demonstrates the type-I isotherms because of the strong adsorbent-adsorbate

interactions [45, 46]. In contrast, the N_2 adsorption desorption isotherms indicate a typical IV-class isotherm with H3-type [47] employing the ZIF-8 under the same conditions as shown in **Figure 5(a)**. Besides this, ZIF8@ZIF67 shows the surface area of 2500 m^2/g, which is much higher than that of ZIF67@ZIF8 (1710 m^2/g), ZIF-8 (1210 m^2/g) and ZIF67 (731 m^2/g). Remarkably, the larger surface area facilitates by the larger surface contact between the electrolyte and electrode to improve the ion electron transfer and thus resulting in improvement of electrochemical activity [48, 49]. Furthermore, the pore size distribution as well as pore volume was determined by means of BJH profiles and the results are illustrated in **Figure 5(b)**. Based on the BJH calculations, the pore diameter for the ZIF-8, ZIF-67, ZIF67@ZIF8 and ZIF8@ZIF67 nanostructures were found to be 1.134, 1.93, 1.0134 and 0.6434 nm, meanwhile their respective pore volume values were 0.695, 0.0257, 0.2035 and 0.3275, cm^3/g, respectively. For these reasons, ZIF8@ZIF67 nanostructures with larger surface area and mesoporous behaviour area not only provide more active sites but also enable the electrolyte penetration during the electrochemical reactions and ion transport due to the more diffusion paths, therefore resulting in substantial enhancement in energy storage applications, in particular supercapacitor [50, 51].

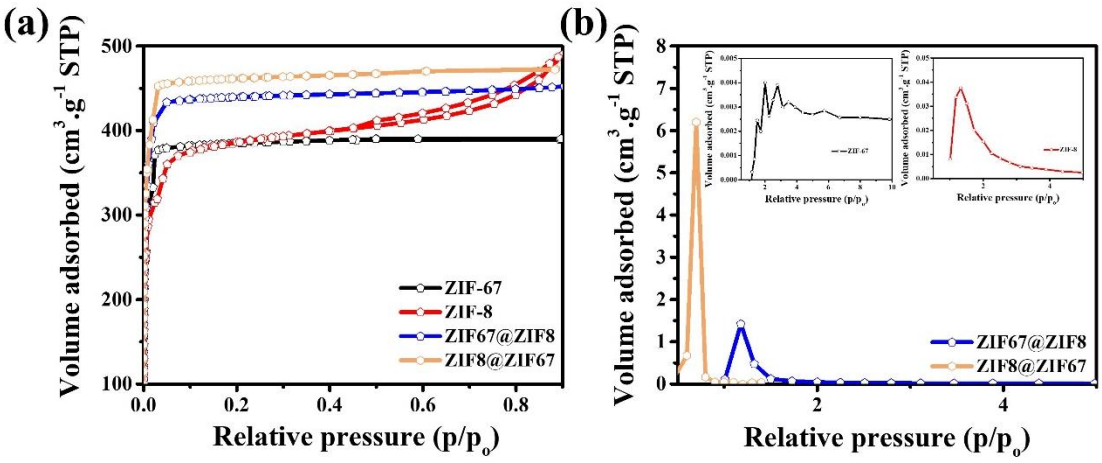

Figure 5*. Surface properties of ZIF-8, ZIF-67, ZIF67@ZIF8 and ZIF8@ZIF67 nanostructures such as* ***(a)*** *Adsorption-desorption isotherms and* ***(b)*** *BJH profiles.*

3.2. Electrochemical characterization of half-cell in 1 M KOH

The electrochemical performance of the ZIF-8, ZIF-67, ZIF67@ZIF8 core-shell and ZIF8@ZIF67 reverse core-shell were analyzed by means of SP150 Biologic Potentiostat. A three-electrode assembly was employed to evaluate the electrochemical behaviour of all the as-prepared samples in 1 M KOH aqueous electrolyte at the potential window of 0.1 to 0.6 V. The CV of all the mentioned electrodes with diverse sweep speed reveals a set of reduction and oxidation peaks in **Figure 6(a-d)**, which exhibits the faradaic nature present in all the materials [52]. In addition, the CV plots demonstrates an improvement of current by retaining its shapes while increasing the sweep rate exhibiting an excellent capacitive nature of the electrode materials and fast diffusion of electrolyte ions to the electrode surface [53]. Likewise, the as-prepared electrodes with dominating redox peaks displays a rapid shift while boosting the sweep rates, demonstrating the outstanding rate

capability of the electrode materials [54]. The CV plots of ZIF-8, ZIF-67, ZIF8@ZIF67 and ZIF67@ZIF8 at a fixed sweep speed of 5 mV/s are displayed in **Figure 6(e)**. Among all, the ZIF67@ZIF8 exhibited the largest CV-loop integrated area and superior current response, and hence overall, delivered excellent electrochemical performance. To further ascertain the electrochemical results, the GCD study was performed for the ZIF8, ZIF67, ZIF67@ZIF8 and ZIF8@ZIF67 electrodes in the applied potential window of 0 to 0.6 V under 1 M KOH electrolyte. Significantly, the GCD test was performed at the various current densities (1, 3, 4, 5, 7, 10 and 13 A/g) by employing all the electrodes; the results are shown in **Figure 6(f-i)**.

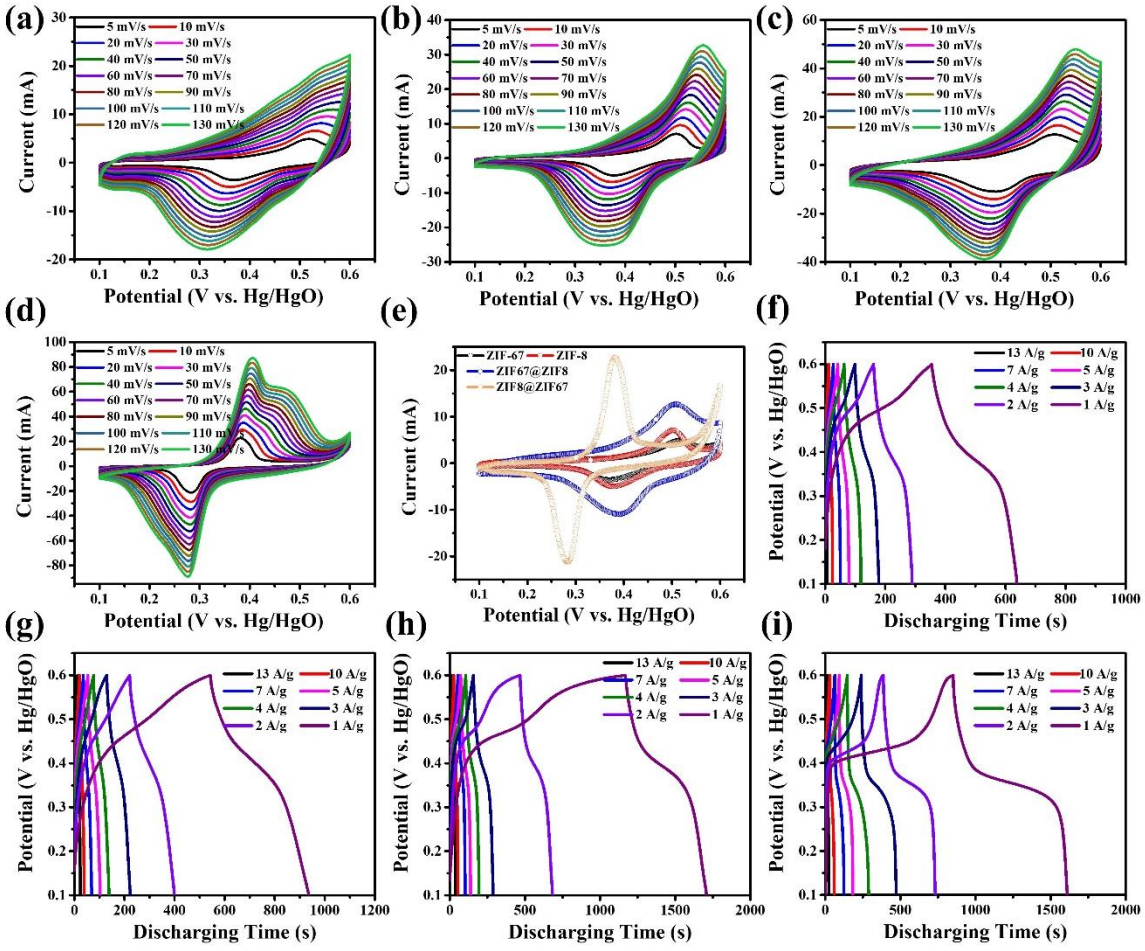

Figure 6. *Electrochemical measurements in the three-electrode configurations for the* ***(a-d)*** *Cyclic voltammogram (CV) plots for the ZIF-67, ZIF-8, ZIF67@ZIF8 and ZIF8@ZIF67 nanostructures under different sweep rates ranging from 5-130 mV/s, respectively,* ***(e)*** *comparative CV profiles for the ZIF-67, ZIF-8, ZIF67@ZIF8 and ZIF8@ZIF67 nanostructure electrodes at the applied fixed sweep speed of 5 mV/s and* ***(f-i)*** *galvanostatic charging-discharging (GCD) profiles for the ZIF-67, ZIF-8, ZIF67@ZIF8 and ZIF8@ZIF67 nanostructured electrodes under a diverse current densities of 1, 2, 3, 4, 5, 7, 10 and 13 A/g, respectively.*

Owing to the presence of the redox reaction, all the electrodes exhibits non-linear GCD plots. **Figure 7(a)** exhibits the comparison of GCD plots of as-prepared electrodes at the constant current density of 1 A/g. The optimized ZIF8@ZIF67 electrode had a longest discharging time compared to other electrodes at the lowest current density, which can assurance the highest C and had a strong agreement with the CV plots. The C of all the as-constructed electrodes were calculated using equation 1 and the values are assessed to the discharge time from the GCD plots at the various applied current densities. Their corresponding C as a function of the applied current densities are demonstrated in **Figure 7 (b)**. The assessed C values of the ZIF8@ZIF67 electrode was 1521, 1392, 1332, 1140, 915, 840, 660 and 585 F/g at the applied current densities of the 1, 2, 3, 4, 5, 7, 10 and 13 A/g, respectively. Likewise, the capacities of the ZIF67@ZIF8 were 1097, 877.7, 804.1, 748, 634, 582, 548.5, 490.2 F/g and the values 788.3, 733.3, 585, 506.6, 450, 396.6, 333.3, and 393 F/g for the ZIF-8 under the current densities of 1-13 A/g. The ZIF-67 showed the lower C values of

571.6, 520, 460, 413.3, 350, 291.6, 266.6 and 216 F/g under the same conditions as those of all the as-constructed electrodes. This raised C of the ZIF8@ZIF67 reverse core-shell electrode might be credited to thorough utilization of the electrochemically active electrode during the charging and discharging process. Moreover, the high capacitance values of the ZIF67@ZIF8 electrode owing to the larger surface area (2500 m^2/g) and uniform morphology compared with other electrodes, considerably offered the abundant channels for the quick diffusion and thus facilitation of electrolyte ions into its inner portion and significantly improved its electrochemical overall performance [5, 55]. In addition, the obtained results of the ZIF8@ZIF67 core-shell electrode showed higher performance even the previously reported the state-of-the art literature (**Table S1**).

Based on the above findings, we can presume that the ZIF8@ZIF67 core-shell electrode had the highest C at the low and high current densities. It is remarked that the C decreased with the raise in discharge current density. In this case, oxidation/reduction reactions are primarily governed by inclusion or exclusion of electrolyte ions into or out from KOH solution of the electrode materials. This is to reveal that the variation in current density has influenced the diffusion of electrolyte ions onto the surface of the electrode materials. The electrolytic ions have considered the visible surface only and not the overall material because of which the whole material is not employed for the redox reactions under the higher current density. This difference, resultantly, is attributed to the decline in charging-discharging times

and consequently the C is reduced.

To further justify the charge-transfer resistance, reaction kinetics and interfacial electrochemistry, EIS analysis was carried out in the frequency range of 10 MHz-100 kHz over the open circuit voltage of 5 mV. As it is evident in **Figure 7(c)**, all the as-constructed electrodes demonstrated an identical trend, comprising a small arc-diameter in the high frequency regions and an inclined prickle in the low frequency section. It is well identified that the smaller arc diameter can possibly ascribed to the charge transfer resistance (R_{ct}) in the high frequency region, likewise the inclined prickle can be attributed to the Warburg resistance in the low frequency region the slope angle of 45°. Significantly, the arc-diameter of the smaller semi-circle in the high frequency region was employed to assess the R_{ct} values of the corresponding electrodes, and the assessed R_{ct} values were 5.78, 9.01, and 11.49 Ω for the for the ZIF8@ZIF67, ZIF67@ZIF8, ZIF-8 and ZIF-67 electrodes. The solution resistance (R_s) of the respective electrodes were recognized from the first intercept of the Nyquist plots with respect to the *X*-axis, and the estimated R_s values were 0.66, 1.30, and 1.53 Ω, respectively, for the ZIF8@ZIF67, ZIF67@ZIF8, ZIF-8 and ZIF-67 electrodes. Manifestly, the calculated R_{ct} and R_s values of ZIF8@ZIF67 electrode is considerably lower compared with other as-constructed electrodes, which undoubtedly signifies the superior intrinsic conducting properties and enhanced the redox electrochemistry.

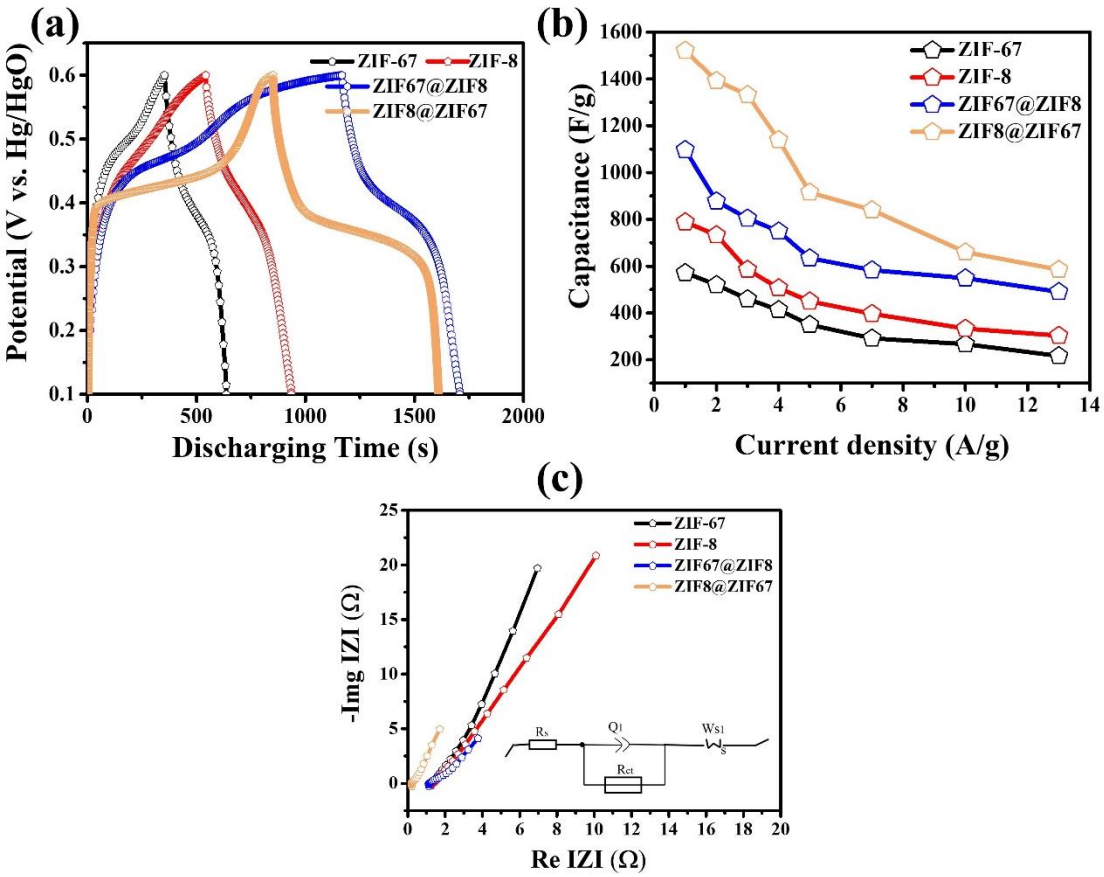

Figure 7. *Electrochemical performance in the three-electrode configuration;* ***(a)*** *comparative GCD profiles for the ZIF-67, ZIF-8, ZIF67@ZIF8 and ZIF8@ZIF67 nanostructure electrodes at the applied fixed current density of 1 A/g and* ***(b)*** *Summary of the specific capacitance of the ZIF-67, ZIF-8, ZIF67@ZIF8 and ZIF8@ZIF67 nanostructure electrodes as a function of the different current densities and* ***(c)*** *Nyquist plot with fitted equivalent circuit (inset).*

3.3. Characterization of a symmetric supercapacitor behaviour in 1 M KOH

To further explore the practical applications of the supercapacitor, a symmetric supercapacitor (SSCs) device was fabricated with the help of two optimized electrodes (ZIF67@ZIF8; core-shell & ZIF8@ZIF67; reverse core-shell) and along with the equivalent mass ratio in 1 M KOH electrolyte. In this study, the effective and stable working potential window was identified to be 0 to 1.4 V due to the limiting

arising from the oxygen evolution when the potential higher than 1.4 V, as the corresponding CV results are depicted in **Figure 8(a)**. Significantly, the CV plot does not include any oxygen or hydrogen evolution peaks at the highest potential of 1.4 V, which indicates that it possesses stable energy storage characteristics. For this reason, the potential window was fixed in 1 M KOH electrolyte for further electrochemical measurements of the SSCs devices. To further investigate the consistency of the optimized SSCs, the CV and GCD measurements as the function of the sweep rates and current density in the voltage range of 0-1.4 V. As shown in **Figure 8(b)**, the CV plots of the ZIF67@ZIF8 and ZIF8@ZIF67 SSCs devices at the fixed sweep speed of 5 mV/s was performed. The integrated area of the ZIF8@ZIF67 was reasonably larger compared with the ZIF67@ZIF8, suggesting that the core-shell hybrid showed the maximum electrochemical outcomes. Significantly, the CV study at the distinct sweep rates (executing from 5 to 90 mV/s) by employing the ZIF8@ZIF67 SSCs were authenticated, and the results are shown in **Figure 8(c)**. Likewise, the CV performance was also examined for the ZIF67@ZIF8 SSCs under the diverse sweep rates from 5 to 90 mV/s, and the results are shown **Figure S5**. The entire CV plot displayed the quesi-rectangular shape with the little hemp during charging and discharging process, and the CV current response enhanced as the sweep rate increased. Therefore, this kind of behaviour attributed to the combination of the pseudocapacitance and EDLC characteristics in both cases (i.e., ZIF8@ZIF67 and ZIF67@ZIF8), which is suggested as hybrid supercapacitor. **Figure 8(d)** illustrates the

CV profiles of the ZIF8@ZIF67 at the 20 mV/s of scan rate over 100 consecutive cycles, and the CV shape did not alter even after the implications of 100 cycles, which confirms that the fabricated SSCs device is highly stable.

The GCD plots of the ZIF8@ZIF67 and ZIF67@ZIF8 SSCs under a fixed current density of 1 A/g within the potential window of 0 to 1.4 V in 1 M KOH electrolyte was presented in **Figure 8(e)**. As expected, the ZIF8@ZIF67 core-shell SSCs showed the longest discharging time while measuring the GCD test at the 1 A/g of current density compared with the ZIF67@ZIF8 reverse core-shell SSCs, suggesting a higher capacitance and the obtained results are being consistent with the CV results. When the applied current increased the GCD plots, the identical shape of the GCD plots of the ZIF67@ZIF8 and ZIF8@ZIF67 SSCs were obtained even at the higher current density with the diverse Δt values, respectively, which further confirms the excellent reversibility and coulomb's efficiency of the as-constructed the SSCs devices (**Figure S6-S7**). The C was determined employing the equation 2 and the values were found to be 249.8, 226.2, 212.1, 169.1, 133.5, 110, 78.4 and 61.5 F/g for the ZIF8@ZIF67 at the 1, 2, 3, 4, 5, 7, 10 and 13 A/g of current densities, respectively and which is considerably higher than that of ZIF67@ZIF8 SSCs device (179.1, 154, 127.7, 94.2, 55, 33, 15.7 and 10.2 F/g) under the identical conditions and the results are shown in **Figure 8(f)**.

To further evaluate the facilitated charge transfer in the ZIF8@ZIF67 and

ZIF67@ZIF8 SSCs devices, the EIS was investigated at open circuit voltage. **Figure 8(g)** displays the Nyquist plots of the as-constructed SSCs with the Randle circuit in inset. The R_s and R_{ct} detailed is provided the 3.2 section. Initially, the X-intercept denotes the solution resistance (R_s) facilitated by electrolyte-electrode interface at the low frequency region. The arc semicircle region demonstrate the charge transfer resistance (R_{ct}) in the high frequency region. As exposed in **Figure 8(g)**, the R_s (5.1 Ω) and R_{ct} (5.4 Ω) of ZIF8@ZIF67 core-shell SSCs are the lowest values compared with the ZIF67@ZIF8 (R_s; 10.1 Ω & R_{ct}; 20 Ω). The higher performance of the ZIF8@ZIF67 core-shell SSCs is attributed to the two reasons: (1) The higher surface area of ZIF8@ZIF67 delivers an improved electrolyte/electrode contact area, consequently facilitating the accessibility of extra active sites for the faradaic reaction, signifying the good electrochemical performance and (2) increased the conductivity which can support the better charge diffusion across the interface, thereby resulting the more charge storage.

Another vital parameter evaluating the overall efficiency of the SSCs device is the cycling stability during charging and discharging process to ensure the practical applicability. A cycling stability study was performed over 10,000 GCD repeated cycles at 10 A/g of current density and the resulting plot is depicted in **Figure 8(h)**. Initially, the capacity retention was observed 100% till the GCD plot of ZIF8@ZIF67 SSCs device was repeated for about 3000 times and then drops by 5% of

capacity when the device was recycled exceeded by 5000 times. Likewise, the ZIF8@ZIF67 SSCs device withheld 87% of the total capacitance after 10,000 cycles at 10 A/g of current density, indicating superior cycling stability. The ZIF67@ZIF8 SSCs device showed a slightly lower capacity retention (79% over 10,000 cycles) compared with the ZIF8@ZIF67 SSCs.

The energy (E) and power (P) density of the as-constructed devices was assessed through equations 3 and 4, and the obtained E and P values were manifest in the resultant Ragone plot, as presented in **Figure 8(i)**. The optimized ZIF8@ZIF67 SSCs device yielded the higher E of 61.2 Wh/kg at the P of 1260 W/kg. Furthermore, the device was well-sustained the E of 15.01 Wh/kg at the P of 163800 W/kg. The achieved E and P values were considerably comparable to the reported literature on the ZIF's based SSCs devices and it was rather larger compared with the ZIF67@ZIF8 SSCs device (43.89 Wh/kg at 1260 W/kg). The E of ZIF8@ZIF67 SSCs device in Ragone plot is demonstrated much larger than the previously published state-of the art literature related to the MOF SCs devices [56-64]. Furthermore, the E and P values along with the cycling stability of the as-constructed ZIF8@ZIF67 SSCs device were compared with the reported literature in previously, as summarized in **Table 1**.

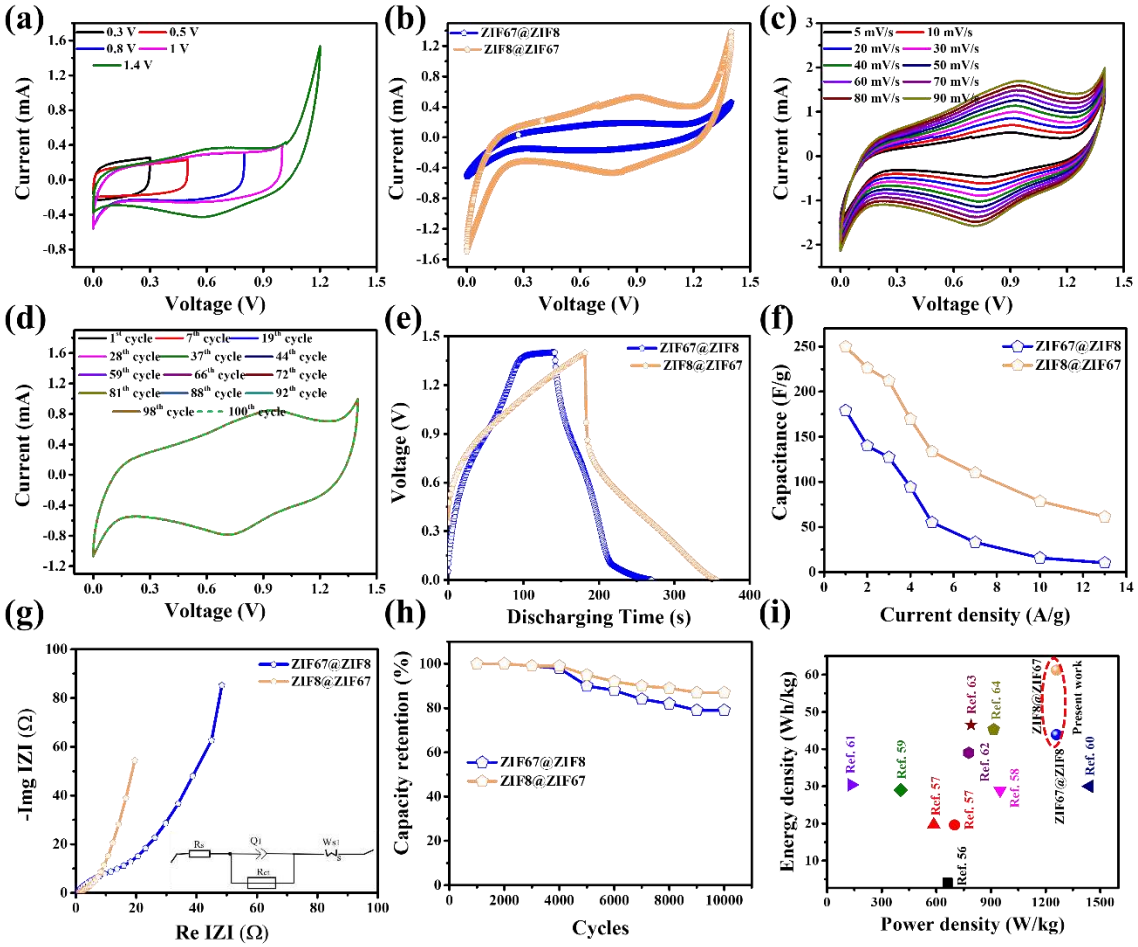

481

482 ***Figure 8.*** *Electrochemical performance of the optimized ZIF67@ZIF8 and ZIF8@ZIF67*
483 *nanostructure SSCs in two-electrode setup;* ***(a)*** *CV profiles at different applied voltages*
484 *under 5 mV/s of scan rate,* ***(b)*** *comparative CV profiles for the ZIF67@ZIF8 and*
485 *ZIF8@ZIF67 nanostructure SSCs at the applied fixed sweep speed of 5 mV/s,* ***(c)*** *CV plots for*
486 *the ZIF67@ZIF8 and ZIF8@ZIF67 nanostructure SSCs under different sweep rates ranging*
487 *from 5-90 mV/s, respectively,* ***(d)*** *CV profiles for the ZIF8@ZIF67 nanostructure SSCs at the*
488 *applied fixed sweep speed of 20 mV/s over 100 cycles,* ***(e)*** *comparative GCD profiles for the*
489 *ZIF67@ZIF8 and ZIF8@ZIF67 nanostructure SSCs under a constant current densities of 1*
490 *A/g,* ***(f)*** *specific capacitance as a function of the diverse current densities,* ***(g)*** *Nyquist plots*
491 *for the ZIF67@ZIF8 and ZIF8@ZIF67 nanostructure SSCs,* ***(h)*** *cyclin stability: capacity*
492 *retention as a function of 10,000 GCD cycles and* ***(i)*** *Ragone plot.*

493

494 **Table 1.** Comparable electrochemical performance of various ZIF's based materials in a two-
495 electrode system.

Electrode Material	Electrolyte	C_s (F/g)/Current Density (A/g)	Power Density (W/kg)	Energy Density (W.h/kg)	Cyclic Stability (%)	Ref
ZIF8@ZIF67	**1 M KOH**	**249.8/1**	**1260**	**61.2**	**87/ 10k**	**This**
ZIF67@ZIF8	**1 M KOH**	**179.11**	**1260**	**43.89**	**79/ 10k**	**work**
ZIF-67@NPC-800	0.5 M H_2SO_4	62 / 2	700	19.6	---	[57]
ZADV@LSC	----------	250 F/g @ 0.8 A/g	586	19.7	89/5000	
ZIF-67@M-Co_3O_4	2 M KOH	134 / 1	790.7	46.5	86.4/8000	[63]
ZIF-67@Co_3O_4-CeO_2	3 M KOH	139.9 / 1	849.9	54.9	98/ 6000	[65]
ZIF-67@3D hollow $CoWO_4$	2 M KOH	81 / 0.5	404	29	---	[59]
$NiCo_2O_4$/MnO_2//Biochar	6 M KOH	85 /1	133.5	30.4	85/5000	[61]
$NiCo_2O_4$/CoFe	2 M KOH	64.7 /1	950	28.9	76.9/5000	[58]
2Fe_2O_3/RGO/Fe_3O_4	2 M KOH	6.9 /20	661.5	4.1/	97/2000	[56]
MO:ZnO@NF//AC	3 M KOH	125.2 /1	778	39	75.6/8000	[62]

496

Conclusion

In summary, the ZIF8@ZIF67 reverse core shell nanostructure with an excellent surface area and uniform hexagonal structure provides a platform for supercapacitor applications. Besides, the ZIF-67, ZIF-8 and ZIF67@ZIF8 core-shell nanostructures were used as reference electrodes. The electrochemical performance was analyzed employing these prepared electrodes with 1 M KOH electrolyte. Among all, the ZIF8@ZIF67 reverse core-shell nanostructure exhibits the high-capacity of 1521 F/g at 1 A/g in three-electrode assembly compared with the ZIF67@ZIF8 (1097 F/g), ZIF-8 (788 F/g) and ZIF-67 (571 F/g). Basis on the preliminary studies, the ZIF67@ZIF8 and ZIF8@ZIF67 was then embedded into the SSCs in a two-electrode setup with 1 M KOH electrolyte. As expected, the ZIF8@ZIF67 reverse core-shell nanostructure displayed the maximum capacitance of 249.8 F/g, high energy and power density of 61.2 Wh/kg and 1260 W/kg under 1 A/g of current density than that of ZIF67@ZIF8. Significantly, the fabricated ZIF8@ZIF67 SSCs delivers a noticeable repeatability of 87% over consecutive 10,000 GCD cycles at 10 A/g of current density. The high performance of the ZIF8@ZIF67 is attributed to the uniform hexagonal like morphology and higher surface area. All the resultant outcomes demonstrate that the ZIF8@ZIF67 core-shell nanocomposite have the considerable potential to be employed as electrode in supercapacitors and other energy related systems.

Conflicts of interest

There are no conflicts to declare.

Acknowledgments

This study was partly supported by the Korea Institute of Energy Technology Evaluation and Planning (KETEP; 20212050100010) and the Technology Innovation Program (20017464) funded by the Ministry of Trade, Industry & energy (MOTIE, Korea) and the National of Korea (NRF) grant (No.2019R1F1A1063622) funded by the Korea government (MSIT).

Reference

[1] G. Xu, P. Nie, H. Dou, B. Ding, L. Li, and X. Zhang, "Exploring metal organic frameworks for energy storage in batteries and supercapacitors," *Materials today,* vol. 20, no. 4, pp. 191-209, 2017.

[2] S. Hussain *et al.*, "MoS2@ X2C (X= Mo or W) hybrids for enhanced supercapacitor and hydrogen evolution performances," *Chemical Engineering Journal,* vol. 421, p. 127843, 2021.

[3] B. Dunn, H. Kamath, and J.-M. Tarascon, "Electrical energy storage for the grid: a battery of choices," *Science,* vol. 334, no. 6058, pp. 928-935, 2011.

[4] C. Guo *et al.*, "Approach of fermi level and electron-trap level in cadmium sulfide nanorods via molybdenum doping with enhanced carrier separation for boosted photocatalytic hydrogen production," *Journal of Colloid and*

Interface Science, vol. 583, pp. 661-671, 2021.

[5] I. Rabani, J. Yoo, H.-S. Kim, S. Hussain, K. Karuppasamy, and Y.-S. Seo, "Highly dispersive Co 3 O 4 nanoparticles incorporated into a cellulose nanofiber for a high-performance flexible supercapacitor," *Nanoscale,* vol. 13, no. 1, pp. 355-370, 2021.

[6] I. Rabani, R. Zafar, K. Subalakshmi, H.-S. Kim, C. Bathula, and Y.-S. Seo, "A facile mechanochemical preparation of Co3O4@ g-C3N4 for application in supercapacitors and degradation of pollutants in water," *Journal of Hazardous Materials,* vol. 407, p. 124360, 2021.

[7] I. Rabani, J. Yoo, C. Bathula, S. Hussain, and Y.-S. Seo, "The role of uniformly distributed ZnO nanoparticles on cellulose nanofibers in flexible solid state symmetric supercapacitors," *Journal of Materials Chemistry A,* vol. 9, no. 19, pp. 11580-11594, 2021.

[8] I. Rabani, K. Karuppasamy, D. Vikraman, H.-S. Kim, and Y.-S. Seo, "Hierarchical structured nano-polyhedrons of CeO2@ ZIF-8 composite for high performance supercapacitor applications," *Journal of Alloys and Compounds,* vol. 875, p. 160074, 2021.

[9] D. Vikraman *et al.*, "Mixed-phase MoS2 decorated reduced graphene oxide hybrid composites for efficient symmetric supercapacitors," *International Journal of Energy Research,* vol. 45, no. 6, pp. 9193-9209, 2021.

[10] I. Rabani, A. Younus, S. Patil, and Y.-S. Seo, "Fabrication of Fe 3 O 4-

incorporated MnO 2 nanoflowers as electrodes for enhanced asymmetric supercapacitor performance," *Dalton Transactions,* vol. 51, no. 37, pp. 14190-14200, 2022.

[11] I. Rabani, Y.-J. Park, J.-W. Lee, M. S. Tahir, A. Kumar, and Y.-S. Seo, "Ultra-thin flexible paper of BNNT–CNF/ZnO ternary nanostructure for enhanced solid-state supercapacitor and piezoelectric response," *Journal of Materials Chemistry A,* vol. 10, no. 29, pp. 15580-15594, 2022.

[12] J. Yoo, M. S. Tahir, I. Rabani, and Y.-S. Seo, "Fabrication of multilayer film with graphene oxide of different surface charge through electrospray deposition," *Applied Surface Science,* vol. 599, p. 153977, 2022.

[13] I. Rabani, M. S. Tahir, F. Afzal, H. B. Truong, M. Kim, and Y.-S. Seo, "High-efficient mineralization performance of photocatalysis activity towards organic pollutants over ruthenium nanoparticles stabilized by metal organic framework," *Journal of Environmental Chemical Engineering,* vol. 11, no. 1, p. 109235, 2023.

[14] I. Rabani *et al.*, "Structural engineering of ruthenium decorated zeolitic imidazole framework nanocomposite for hydrogen evolution reactions and supercapacitors," *Journal of Energy Storage,* vol. 62, p. 106885, 2023.

[15] M. S. Tahir *et al.*, "Analysis of the porosity of ZIF-8 and ZIF-8@ CNF membranes using positron annihilation lifetime spectroscopy (PALS)," *Journal of Radioanalytical and Nuclear Chemistry,* pp. 1-9, 2023.

[16] Y. Zhang, S. Yuan, X. Feng, H. Li, J. Zhou, and B. Wang, "Preparation of nanofibrous metal–organic framework filters for efficient air pollution control," *Journal of the American Chemical Society,* vol. 138, no. 18, pp. 5785-5788, 2016.

[17] H. Zheng *et al.*, "One-pot synthesis of metal–organic frameworks with encapsulated target molecules and their applications for controlled drug delivery," *Journal of the American chemical society,* vol. 138, no. 3, pp. 962-968, 2016.

[18] W. Zhang *et al.*, "Site-Selective Catalysis of a Multifunctional Linear Molecule: The Steric Hindrance of Metal–Organic Framework Channels," *Advanced Materials,* vol. 30, no. 23, p. 1800643, 2018.

[19] W. Xia, A. Mahmood, R. Zou, and Q. Xu, "Metal–organic frameworks and their derived nanostructures for electrochemical energy storage and conversion," *Energy & Environmental Science,* vol. 8, no. 7, pp. 1837-1866, 2015.

[20] H. B. Wu and X. W. Lou, "Metal-organic frameworks and their derived materials for electrochemical energy storage and conversion: Promises and challenges," *Science Advances,* vol. 3, no. 12, p. eaap9252, 2017.

[21] P.-Y. Lee and L.-Y. Lin, "Investigating energy storage ability of ZIF67-derived perovskite fluoride via tuning ammonium fluoride amounts," *Journal of Alloys and Compounds,* vol. 892, p. 162191, 2022.

[22] P.-Y. Lee, L.-Y. Lin, I.-J. Hsu, C.-Y. Chan, J.-F. Lee, and H.-S. Sheu, "Facile

synthesis of perovskite ZIF67 derivative using ammonia fluoride and comparison with post-treated ZIF67 derivatives on energy storage ability," *Electrochimica Acta,* vol. 389, p. 138680, 2021.

[23] A. M. Mohamed, A. O. Abo El Naga, T. Zaki, H. B. Hassan, and N. K. Allam, "Bimetallic Co–W–S chalcogenides confined in N, S-codoped porous carbon matrix derived from metal–organic frameworks for highly stable electrochemical supercapacitors," *ACS Applied Energy Materials,* vol. 3, no. 8, pp. 8064-8074, 2020.

[24] T.-R. Kuo, L.-Y. Lin, K.-Y. Lin, and S. Yougbaré, "Effects of size and phase of TiO2 in poly (vinyl alcohol)-based gel electrolyte on energy storage ability of flexible capacitive supercapacitors," *Journal of Energy Storage,* vol. 52, p. 104773, 2022.

[25] T.-R. Kuo *et al.*, "Novel synthesis of ZIF67 derived cobalt and nickel oxides induced by ammonium tetrafluoroborate as electroactive material of battery supercapacitor hybrids," *Journal of Energy Storage,* vol. 68, p. 107831, 2023.

[26] P.-Y. Lee, S.-C. Wang, S. Yougbaré, L.-Y. Lin, and J. Gong, "Designing ZIF67 derivatives using ammonia-based fluorine complex as structure-directing agent for energy storage applications," *Journal of Power Sources,* vol. 576, p. 233230, 2023.

[27] C.-H. Wu, Y.-F. Wu, P.-Y. Lee, S. Yougbaré, and L.-Y. Lin, "Ligand incorporating sequence-dependent ZIF67 derivatives as active material of

supercapacitor: competition between ammonia fluoride and 2-methylimidazole," *ACS Applied Materials & Interfaces,* vol. 14, no. 38, pp. 43180-43194, 2022.

[28] P.-Y. Lee, T.-M. Cheng, S. Yougbaré, and L.-Y. Lin, "Design of novel self-assembled MXene and ZIF67 derivative composites as efficient electroactive material of energy storage device," *Journal of Colloid and Interface Science,* vol. 618, pp. 219-228, 2022.

[29] Z. Ma *et al.*, "The methodologically obtained derivative of ZIF-67 metal–organic frameworks present impressive supercapacitor performance," *New Journal of Chemistry,* vol. 46, no. 15, pp. 7230-7241, 2022.

[30] A. Rahim, S. R. Majid, C.-K. Sim, S. Yusuf, and Z. Osman, "Synthesis and electrochemical evaluation of cobalt-based ZIF-67 with its potential as direct use electrode materials for supercapacitors," *Journal of Industrial and Engineering Chemistry,* vol. 100, pp. 248-259, 2021.

[31] S.-C. Wang *et al.*, "Novel synthesis of ammonia borane fluoride induced ZIF67 derivatives using facile one-step solution process for energy storage," *Materials Today Chemistry,* vol. 32, p. 101619, 2023.

[32] L. Wang, H. Yang, G. Pan, L. Miao, S. Chen, and Y. Song, "Polyaniline-carbon nanotubes@ zeolite imidazolate framework67-carbon cloth hierarchical nanostructures for supercapacitor electrode," *Electrochimica Acta,* vol. 240, pp. 16-23, 2017.

[33] S. Sundriyal, V. Shrivastav, H. Kaur, S. Mishra, and A. Deep, "High-performance symmetrical supercapacitor with a combination of a ZIF-67/rGO composite electrode and a redox additive electrolyte," *ACS omega,* vol. 3, no. 12, pp. 17348-17358, 2018.

[34] S. Zhou, X. Kong, B. Zheng, F. Huo, M. Strømme, and C. Xu, "Cellulose nanofiber@ conductive metal–organic frameworks for high-performance flexible supercapacitors," *ACS nano,* vol. 13, no. 8, pp. 9578-9586, 2019.

[35] R. Banerjee *et al.*, "High-throughput synthesis of zeolitic imidazolate frameworks and application to CO2 capture," *Science,* vol. 319, no. 5865, pp. 939-943, 2008.

[36] I. Rabani *et al.*, "Tunning the Zeolitic Imidazole Framework (ZIF8) through the Wet Chemical Route for the Hydrogen Evolution Reaction," *Nanomaterials,* vol. 13, no. 10, p. 1610, 2023.

[37] M. Shahsavari, M. Mortazavi, S. Tajik, I. Sheikhshoaie, and H. Beitollahi, "Synthesis and characterization of GO/ZIF-67 nanocomposite: investigation of catalytic activity for the determination of epinine in the presence of dobutamine," *Micromachines,* vol. 13, no. 1, p. 88, 2022.

[38] A. Schejn *et al.*, "Cu 2+-doped zeolitic imidazolate frameworks (ZIF-8): efficient and stable catalysts for cycloadditions and condensation reactions," *Catalysis Science & Technology,* vol. 5, no. 3, pp. 1829-1839, 2015.

[39] B. Wang *et al.*, "An insight into the initial Coulombic efficiency of carbon-

based anode materials for potassium-ion batteries," *Chemical Engineering Journal,* vol. 428, p. 131093, 2022.

[40] S. Luanwuthi, A. Krittayavathananon, P. Srimuk, and M. Sawangphruk, "In situ synthesis of permselective zeolitic imidazolate framework-8/graphene oxide composites: rotating disk electrode and Langmuir adsorption isotherm," *RSC Advances,* vol. 5, no. 58, pp. 46617-46623, 2015.

[41] Y. Li *et al.*, "Highly Dispersed Metal Carbide on ZIF-Derived Pyridinic-N-Doped Carbon for CO2 Enrichment and Selective Hydrogenation," *ChemSusChem,* vol. 11, no. 6, pp. 1040-1047, 2018.

[42] J. Ran *et al.*, "One-step in-situ growth of zeolitic imidazole frameworks-8 on cotton fabrics for photocatalysis and antimicrobial activity," *Cellulose,* vol. 27, pp. 10447-10459, 2020.

[43] R. Zhu *et al.*, "Quasi-ZIF-67 for boosted oxygen evolution reaction catalytic activity via a low temperature calcination," *ACS applied materials & interfaces,* vol. 12, no. 22, pp. 25037-25041, 2020.

[44] L. Ma, X. Zhang, M. Ikram, M. Ullah, H. Wu, and K. Shi, "Controllable synthesis of an intercalated ZIF-67/EG structure for the detection of ultratrace Cd2+, Cu2+, Hg2+ and Pb2+ ions," *Chemical Engineering Journal,* vol. 395, p. 125216, 2020.

[45] M. Kruk and M. Jaroniec, "Gas adsorption characterization of ordered organic− inorganic nanocomposite materials," *Chemistry of materials,* vol. 13,

686 no. 10, pp. 3169-3183, 2001.
687 [46] Z. Li *et al.*, "Thin-film electrode based on zeolitic imidazolate frameworks
688 (ZIF-8 and ZIF-67) with ultra-stable performance as a lithium-ion battery
689 anode," *Journal of Materials Science,* vol. 52, pp. 3979-3991, 2017.
690 [47] R. S. Gohar *et al.*, "Hydrothermal preparation of LaNdZr2O7–SnSe
691 nanocomposite for electrochemical supercapacitor and degradation of
692 contaminants' applications," *Journal of Energy Storage,* vol. 52, p. 104930, 2022.
693 [48] R. Tian *et al.*, "MOF-derived hollow Co3S4 quasi-polyhedron/MWCNT
694 nanocomposites as electrodes for advanced lithium ion batteries and
695 supercapacitors," *ACS Applied Energy Materials,* vol. 1, no. 2, pp. 402-410, 2018.
696 [49] F. Yuan *et al.*, "Unraveling the effect of intrinsic carbon defects on potassium
697 storage performance," *Advanced Functional Materials,* vol. 32, no. 48, p. 2208966,
698 2022.
699 [50] F. Yuan *et al.*, "Cobalt Nanoparticles Synergize with Oxygen-Containing
700 Functional Groups to Realize Fast and Stable Potassium Storage for Carbon
701 Anode," *Advanced Functional Materials,* p. 2304753, 2023.
702 [51] F. Yuan *et al.*, "Unraveling the intercorrelation between micro/mesopores and
703 K migration behavior in hard carbon," *Small,* vol. 18, no. 12, p. 2107113, 2022.
704 [52] V. Siva, A. Murugan, A. Shameem, S. Thangarasu, S. Kannan, and S. A.
705 Bahadur, "In situ encapsulation of V 2 O 5@ ZIF-8 nanocomposites as
706 electrode materials for high-performance supercapacitors with long term

cycling stability," *Journal of Materials Chemistry C,* vol. 11, no. 8, pp. 3070-3085, 2023.

[53] C. I. Priyadharsini *et al.*, "Sol–Gel synthesis of Co 3 O 4 nanoparticles as an electrode material for supercapacitor applications," *Journal of Sol-Gel Science and Technology,* vol. 96, pp. 416-422, 2020.

[54] B. Pandit, D. P. Dubal, P. Gómez-Romero, B. B. Kale, and B. R. Sankapal, "V2O5 encapsulated MWCNTs in 2D surface architecture: complete solid-state bendable highly stabilized energy efficient supercapacitor device," *Scientific Reports,* vol. 7, no. 1, pp. 1-12, 2017.

[55] R. Heimböckel, F. Hoffmann, and M. Fröba, "Insights into the influence of the pore size and surface area of activated carbons on the energy storage of electric double layer capacitors with a new potentially universally applicable capacitor model," *Physical Chemistry Chemical Physics,* vol. 21, no. 6, pp. 3122-3133, 2019.

[56] C. Zhao, X. Shao, Y. Zhang, and X. Qian, "Fe2O3/reduced graphene oxide/Fe3O4 composite in situ grown on Fe foil for high-performance supercapacitors," *ACS applied materials & interfaces,* vol. 8, no. 44, pp. 30133-30142, 2016.

[57] N. L. Torad *et al.*, "Electric double-layer capacitors based on highly graphitized nanoporous carbons derived from ZIF-67," *Chemistry–A European Journal,* vol. 20, no. 26, pp. 7895-7900, 2014.

[58] W. Chen *et al.*, "Hierarchical NiCo2O4@ Co-Fe LDH core-shell nanowire arrays for high-performance supercapacitor," *Applied Surface Science,* vol. 451, pp. 280-288, 2018.

[59] D. Chu *et al.*, "3D Hollow Flower-like CoWO4 Derived from ZIF-67 Grown on Ni-foam for High-Performance Asymmetrical Supercapacitors," *Chemistry–An Asian Journal,* vol. 15, no. 11, pp. 1750-1755, 2020.

[60] G. Zhao *et al.*, "Flexible nitrogen-doped carbon heteroarchitecture derived from ZIF-8/ZIF-67 hybrid coating on cotton biomass waste with high supercapacitive properties," *Microporous and Mesoporous Materials,* vol. 303, p. 110257, 2020.

[61] B. Ren, M. Fan, X. Yang, L. Wang, and H. Yu, "3D Hierarchical structure Electrodes of MnO2 Nanosheets Decorated on Needle-like NiCo2O4 Nanocones on Ni Foam as a cathode material for Asymmetric Supercapacitors," *ChemistrySelect,* vol. 4, no. 19, pp. 5641-5650, 2019.

[62] A. Ali *et al.*, "Mo-doped ZnO nanoflakes on Ni-foam for asymmetric supercapacitor applications," *RSC advances,* vol. 9, no. 47, pp. 27432-27438, 2019.

[63] G. Wei, Z. Zhou, X. Zhao, W. Zhang, and C. An, "Ultrathin metal–organic framework nanosheet-derived ultrathin Co3O4 nanomeshes with robust oxygen-evolving performance and asymmetric supercapacitors," *ACS applied materials & interfaces,* vol. 10, no. 28, pp. 23721-23730, 2018.

[64] X. Fan *et al.*, "Asymmetric supercapacitors utilizing highly porous metal-organic framework derived Co3O4 nanosheets grown on Ni foam and polyaniline hydrogel derived N-doped nanocarbon electrode materials," *Chemical Physics Letters,* vol. 689, pp. 162-168, 2017.

[65] C. Wei *et al.*, "Self-template synthesis of hybrid porous Co3O4–CeO2 hollow polyhedrons for high-performance Supercapacitors," *Chemistry–An Asian Journal,* vol. 13, no. 1, pp. 111-117, 2018.